Flutter of an elastic plate in a channel flow: confinement and finite-size effects

Olivier Doaré[a], Martin Sauzade[a], Christophe Eloy[b]

[a]*ENSTA Paristech, Unité de Mécanique, Chemin de la Hunière, 91761 Palaiseau, France*
[b]*IRPHE, CNRS & Aix-Marseille Université, 49 rue Joliot-Curie, 13013 Marseille, France*

Abstract

When a cantilevered plate lies in an axial flow, it is known to exhibit self-sustained oscillations once a critical flow velocity is reached. This flutter instability has been investigated theoretically, numerically and experimentally by different authors, showing that the critical velocity is always underestimated by two-dimensional models. However, it is generally admitted that if the plate is confined in the spanwise direction by walls, three-dimensionality of the flow is reduced and the two-dimensional models can apply. The aim of this article is to quantify this phenomenon by analyzing the effect of the clearance between the plate and the side walls on the flutter instability. To do so, the pressure distribution around an infinite-length plate is first solved in the Fourier space, which allows to develop an empirical model for the pressure jump. This empirical model is then used in real space to compute instability thresholds as a function of the channel clearance, the plate aspect ratio and mass ratio. Our main result shows that, as the value of the clearance is reduced, the convergence towards the two-dimensional limit is so slow that this limit is unattainable experimentally.

Keywords: Flow-induced vibration, Cantilevered plate, Flutter instability, Channel flow.

1. Introduction

Cantilevered plates in axial flow are known to exhibit self-sustained oscillations once a critical flow velocity is reached. This phenomenon has been the main focus of a large amount of studies, motivated by applications in biomechanics (Aurégan and Depollier, 1995; Huang, 1995), paper industry (Watanabe et al., 2002b), aerospace and nuclear engineering (Guo and Paidoussis, 2000) or aeronautics (Kornecki et al., 1976). Plates are usually differentiated from flags through the restoring force that maintains the structure in the flat equilibrium position. The restoring force is due to elastic bending rigidity for plates, while it is a tensile force induced by fluid friction and flag weight in the flag case.

Email address: olivier.doare@ensta.fr (Olivier Doaré)

A plate of infinite span and infinite length in a potential flow has been proven to be unstable at any non-zero flow velocity (Rayleigh, 1879). It was found since then that taking into account the finite size of the plate (its span and/or chord) tends to stabilize it, so that the critical velocity for flutter instability is no longer zero but has a finite value.

Many studies have considered finite-length and infinite-span plates, which involved a two-dimensional homogeneous flow around the structure, modeled as an Euler-Bernoulli beam. Here, since the flow is considered to be two-dimensional, independent of the spanwise coordinate, this approach is referred to as two-dimensional. In the literature, one can distinguish two methods when solving this problem. The first one, used by Kornecki et al. (1976), introduces circulation around the plate and wake vortices so that the Kutta condition is satisfied at the trailing edge, as done by Theodorsen (1935) in the context of airfoil flutter. Huang (1995) and Watanabe et al. (2002a) used the same modeling and provided complementary results on the linear stability of the plate. The second approach was introduced by Guo and Paidoussis (2000) and consists in imposing continuity of the pressure everywhere except across the plate. The pressure distribution is then solved in the Fourier space, assuming that no singularity exists at both leading and trailing edges of the plate. However, this model implies an incoming "wake" regularizing the flow at the leading edge, which does not happen in real situations. Yet, the two models give very similar results provided the plate is long and flexible enough (Eloy et al., 2008; Michelin and Llewellyn Smith, 2009).

Another asymptotic case can be considered when the plate span is small compared to its chord. This so-called slender-body approach was first introduced by Lighthill (1960) in his seminal paper on fish locomotion and recently applied by Lemaitre et al. (2005) to address the flow-induced instability of slender plates tensioned by gravity.

The flutter of cantilevered plates has been investigated experimentally by Taneda (1968), Datta and Gottenberg (1975), Kornecki et al. (1976), Yamaguchi et al. (2000), Watanabe et al. (2002b) and Eloy et al. (2008). They showed that the deflection of the plate during the self-sustained oscillations is independent of the spanwise coordinate, validating the use of an Euler-Bernoulli beam model for the plate deflection. However, the experimental values of critical velocity was always found to be higher than predicted by the theoretical two-dimensional models. In the case of plates of small aspect ratio, the experiments and slender-body theory have been compared by (Lemaitre et al., 2005). The experimental critical velocity has also been found to be higher than the theoretical one. In other words, plates in the experiments appear invariably more stable than predicted.

Numerical simulations have been carried out to adress the instability threshold in the two-dimensional case. In these simulations the plate is modeled with an Euler-Bernoulli beam equation and the fluid is described either by the Navier-Stokes equations (Watanabe et al., 2002a; Balint and Lucey, 2005; Howell et al., 2009) or using vortex methods (Tang and Païdoussis, 2007; Michelin et al., 2008; Alben and Shelley, 2008). All these simulations recovered the instability thresh-

old of the two-dimensional theoretical models. Additionally, these numerical studies provided a better insight into the instability mechanism and the energy exchange between the fluid and the flexible structure.

The discrepancy between theoretical and experimental values for the critical velocity motivated the development of a three-dimensional model for the fluid flow around the plate (Eloy et al., 2007, 2008). Here, the plate remained modeled by an Euler-Bernoulli beam equation while the three-dimensional flow around the plate was modeled using the same assumptions as in Guo and Paidoussis (2000). This model was found to improve the prediction of critical velocities as well as to provide a unified theory that fills the gap between two-dimensional models and slender-body models.

Most of the works cited above have considered the flutter of a flexible plate in an unbounded flow. Motivated by the study of snoring, some authors however examined the effect of confinement. The two-dimensional problem of a plate of infinite span in a channel flow has been modeled by Aurégan and Depollier (1995) and Guo and Paidoussis (2000) and the channel flow confinement was found to have a destabilizing effect. The limit of extremely low values of the channel width leads to the so called leakage flow instability problem (Wu and Kaneko, 2005). Comparatively, the channel flow confinement in the spanwise direction was overlooked. In his experiments, Huang (1995) mentions a plate that spans over the entire 6cm width of the channel with a small clearance of 2mm on each side, in order to reduce the three-dimensionality of the flow. Aurégan and Depollier (1995) noticed a discrepancy between their two-dimensional theory and experiments, that they attributed to the clearance on the transverse sides of the plate. To overcome this difference, they introduced in their model an effective span 90% smaller than the real span. It is commonly admitted that confining the flow in the spanwise direction limits the three-dimensional effects. However, to the author's knowledge, except the empirical correction proposed by Aurégan and Depollier (1995), this effect has never been addressed quantitatively.

The main objective of this paper is hence to quantify the effect of the clearance between plate and channel walls on the instability thresholds. In section 2, the problem of a finite span, finite chord plate in a finite height, infinite width channel flow will be presented. Equations and boundary conditions satisfied by the potential flow will be developed to obtain an Helmholtz problem for the pressure jump in the Fourier space. This problem will be solved numerically and theoretically in the third section and the data obtained will be used to formulate an empirical model. In section 4, the instability thresholds will be computed as function of the plate aspect ratio and the channel clearance using this empirical model. Finally, the effect of the gap on the critical velocity will be discussed in relation to experiments.

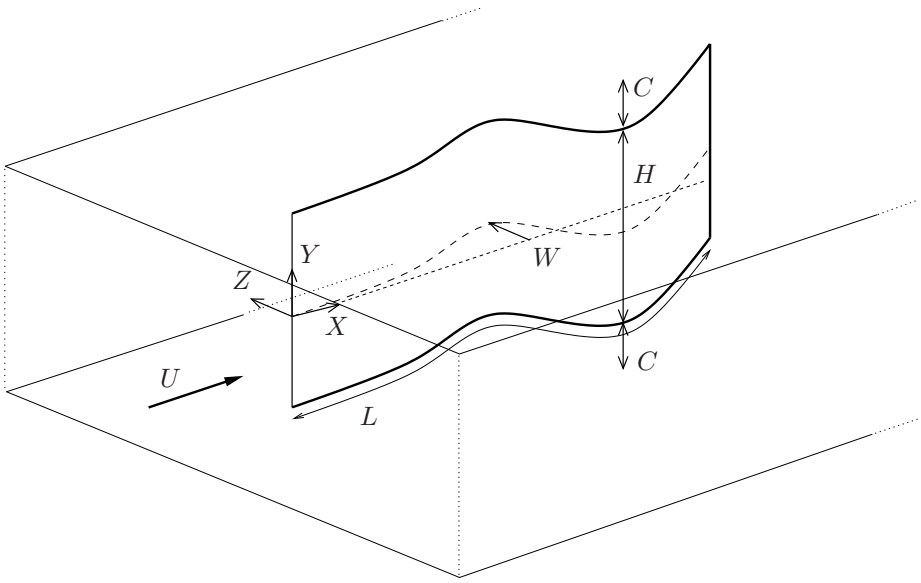

Figure 1: Schematic view of a cantilevered plate in an axial potential flow bounded by two rigid walls.

2. Formulation of the problem

2.1. Equation of motion

As sketched in Fig. 1, a cantilevered plate of length (or chord) L and height (or span) H is considered. The plate is surrounded by an airflow of constant velocity U in the X direction and bounded above and below by rigid walls at a distance $H + 2C$, so that the gap between the plate and the walls is C (also called the clearance in the text). The lateral plate deflection is noted W, and is considered to be independent of the vertical coordinate Y, so that it is governed by the linearized Euler-Bernoulli beam equation with an additional forcing term due to the fluid pressure,

$$MW_{TT} + DW_{XXXX} = \langle [P] \rangle, \tag{1}$$

where D is the flexural rigidity of the plate, M its surface density and $\langle [P] \rangle$ the mean value along the span H of the pressure jump across the plate (the notation $[P]$ stands for $P(Z = 0^+) - P(Z = 0^-)$). Considering a finite length L, boundary conditions will be those of a clamped-free beam, $W = W_X = 0$ in $X = 0$, and $W_{XX} = W_{XXX} = 0$ in $X = L$.

The following dimensionless quantities are introduced

$$x = \frac{x}{L}, \quad y = \frac{Y}{L}, \quad z = \frac{Z}{L}, \quad w = \frac{W}{L}, \quad t = \frac{UT}{L}, \quad p = \frac{P}{\rho U^2}, \tag{2}$$

where ρ is the fluid density, so that the dimensionless equation of motion (1) is

$$w_{tt} + \frac{1}{U^{*2}} w_{xxxx} = M^* \langle [p] \rangle, \tag{3}$$

where U^* and M^* are the reduced velocity and mass ratio, defined as

$$U^* = \sqrt{\frac{M}{D}} LU, \quad M^* = \frac{\rho L}{M}. \tag{4}$$

With this choice of dimensionless parameters, the plate span is $h = H/L$, and the gap is $c = C/L$.

2.2. Potential flow

Assuming a large Reynolds number, the flow around the plate is considered to be potential. For the present linear model, this means that the vorticity is entirely concentrated in the surface $z = 0$, both in the plate itself to model the viscous boundary layers and in its wake where the vorticity is shed with velocity U. Under these hypothesis, the perturbation pressure $p(x, y, z, t)$ and the perturbation potential $\phi(x, y, z, t)$ are related by the unsteady linearized Bernoulli equation

$$p = -(\partial_t + \partial_x)\phi. \tag{5}$$

Boundary conditions are given by the impermeability condition on the walls and on the plate and yields a Neumann problem for the Laplace equation satisfied by the potential ϕ. Applying the operator $(\partial_t + \partial_x)$ on these boundary conditions gives another Neumann problem for the pertubation pressure

$$\begin{aligned} \Delta p &= 0, & (6)\\ [p_y]_{|y|=h/2+c} &= 0, & (7)\\ [p_z]_{z=0} &= -(\partial_t + \partial_x)^2 w \quad \text{for } (x, y) \in \mathbb{D}, & (8) \end{aligned}$$

where $\mathbb{D}$ is the plate area.

2.3. Problem in the Fourier space

To solve the set of equations (6–8), the pressure field is expressed in the Fourier space such that

$$p = \int_{-\infty}^{\infty} \psi(k, y, z) \mathrm{e}^{\mathrm{i}kx} \, \mathrm{d}k, \tag{9}$$

where ψ satisfy the following equations

$$\begin{aligned} (\partial_y^2 + \partial_z^2)\psi &= k^2 \psi, & (10)\\ [\psi_y]_{|y|=h/2+c} &= 0, & (11)\\ [\psi_z]_{z=0} &= v(k) \quad \text{for } |y| < h/2, & (12) \end{aligned}$$

and $v(k)$ is the Fourier transform of $-(\partial_t + \partial_x)^2 w$

$$\int_{-\infty}^{\infty} v(k)\, \mathrm{e}^{\mathrm{i}kx}\, \mathrm{d}k = -(\partial_t + \partial_x)^2 w. \tag{13}$$

The set of equation (10–12) defines the problem in the Fourier space. It is a two dimensional problem where the field ψ is solution of the Helmoltz equation (10) with Neumann boundary conditions (11–12). The problem being linear, for a given wavenumber k, ψ is proportional to $v(k)$ such that the average along the span of the potential jump can always be written in the form

$$\langle [\psi] \rangle = -\frac{2}{k} g(k, h, c)\, v(k). \tag{14}$$

The linear problem given by equations (10–12) will be solved in the next section numerically and theoretically with the aim of evaluating the function $g(k, h, c)$.

Taking the x-derivative of equation (9) and executing an inverse Fourier transform yields

$$\psi = \frac{1}{2\pi \mathrm{i} k} \int_0^1 \partial_x p\, \mathrm{e}^{-\mathrm{i}kx}\, \mathrm{d}x. \tag{15}$$

Taking the jump across the surface $z = 0$ of the above equation and averaging along the span gives

$$\langle [\psi] \rangle = \frac{1}{2\pi \mathrm{i} k} \int_0^1 p'(\xi)\, \mathrm{e}^{-\mathrm{i}k\xi}\, \mathrm{d}\xi, \tag{16}$$

where $p'(x) = \langle [\partial_x p] \rangle$ is the x-derivative of averaged pressure jump. Inserting (14) and (16) into (13) and inverting the integral signs yields the following integral equation for p'

$$\frac{1}{2\pi} \fint_0^1 p'(\xi) G(x - \xi, h, c)\, \mathrm{d}\xi = (\partial_t + \partial_x)^2 w, \tag{17}$$

where

$$G(x, h, c) = \int_0^\infty \frac{\sin(kx)}{g(k, h, c)} \mathrm{d}k, \tag{18}$$

and the bar on the integral sign denotes that the Cauchy principal value should be taken (see Mangler, 1951) as the kernel G has an inverse-power singularity in $x = 0$. Solving the inverse problem (17) and integrating allows to find the averaged pressure distribution for a given motion of the plate $w(x, t)$.

It should be noted that the boundary condition in the Fourier space given by equation (12) is only an approximation. Indeed, the Neumann boundary condition given by equation (8) applies only on the plate area $\mathbb{D}$ and not in the wake. Therefore, when expressed in the Fourier space, $v(k)$ can slightly depend on y in general. The approximation will be accurate however when the wake behind the fluttering plate has the same properties as the flow over the plate. This will be realized when the dimensionless frequency $\omega = \Omega L/U$ is of order unity (where Ω is the angular frequency) or in the asymptotic cases of large and small aspect ratios.

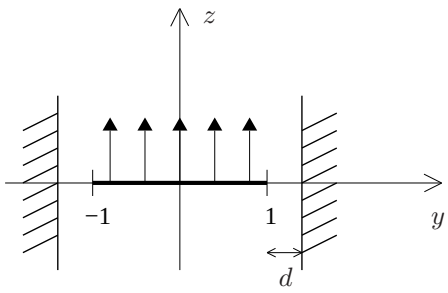

Figure 2: Schematic representation of the problem in the Fourier space.

3. Pressure jump in the Fourier space

In the Fourier space, rescaling all lengths by $h/2$, the rescaled perturbation potential satisfies the following system

$$\Delta\varphi = \kappa^2\varphi, \tag{19}$$

$$[\varphi_y]_{|y|=1+d} = 0, \tag{20}$$

$$[\varphi_z]_{z=0} = 1, \quad \text{for } |y|<1, \tag{21}$$

where $\kappa = kh/2$, $d = 2c/h$ and $\varphi = 2\psi/hv(k)$. The first equation is the Helmoltz equation (the Δ is the Laplace operator in two-dimensions here), and the two others are the boundary conditions on the plate and on the walls. This problem is sketched in Fig. 2.

The goal of this section is to determine the function g now defined as

$$g(\kappa, d) = -\frac{\kappa}{2}\langle[\varphi]\rangle = -\kappa\langle\varphi^+\rangle. \tag{22}$$

where φ^+ is a shortcut for $\varphi(z=0^+)$.

Before solving these equations in the general case, let us recall the results in the two-dimensional and slender-body limit cases when the clearance is infinite. The slender-body limit corresponds to $\kappa \ll 1$ and can be deduced from the results of Lighthill (1960)

$$\varphi^+ \simeq -\sqrt{1-y^2}, \quad \text{for } |y|<1 \text{ and } \kappa \ll 1. \tag{23}$$

The two-dimensional limit corresponds to $\kappa \gg 1$. In this situation, the pressure potential is independent of the spanwise coordinate and the resolution of equations (19-21) yields

$$\varphi^+ \simeq -\frac{1}{\kappa}, \quad \text{for } |y|<1 \text{ and } \kappa \gg 1. \tag{24}$$

3.1. Numerical calculation

Numerical resolution of the Helmoltz problem defined by equations (19–21) is now presented. First of all, the problem has to be of finite size to allow

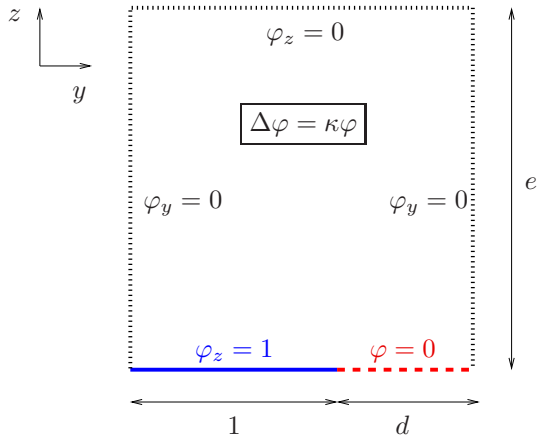

Figure 3: Equations and boundary conditions of the equivalent numerical problem after considering symmetry properties of the original problem.

implementation of a finite element method in the two-dimensional fluid domain. A second gap e in the lateral direction z is hence introduced. The gap e has to be large enough to ensure that the problem solved numerically is equivalent to that of a plate in an infinite width channel. In practice, the value of $e = 30$ was used in the numerical computations presented in the following. This assured that the pressure distribution converged to that of an infinite domain in the z direction at all the explored values of κ and d.

Next, two symmetry properties of the problem may be considered to simplify its numerical resolution. Indeed, the problem, through its boundary conditions, is symmetric with respect to the Oz-axis, and skew-symmetric with respect to the Oy-axis. Due to the inviscid nature of the fluid, the problem is reduced to $y \geq 0$ and $z \geq 0$ as sketched in Fig. 3b. The relevant boundary conditions appear on the figure.

The numerical resolution of this classical Helmoltz problem has been done with the help of the COMSOL software. The explored values of d and κ where in the range $[10^{-4}, 5]$ and $[10^{-4}, 30]$ respectively.

Four typical results for the pressure potential φ are presented in Fig. 4. On this figure, color levels of the quantity $-\kappa\varphi$ are plotted in the fluid domain (figures above), and its value at $z = 0$ is plotted on the graphs below, as function of y, so that the area below this curve corresponds to the function g defined in equation (22). The behavior of $-\kappa\varphi^+$ predicted by the slender-body and two-dimensional models are also plotted. One can make some preliminary observations from these four typical cases. Indeed, comparing cases (a) and (b) shows that increasing κ has for consequence to approach the two-dimensional limit. Comparison of cases (b) and (c) shows that decreasing d towards zero has the same effect. It appears however that even for a value of d as small as 10^{-4}, the numerical result differs significantly from the two-dimensional limit, when $\kappa = 1$. Finally, difference between cases (b) and (d) illustrates the fact that

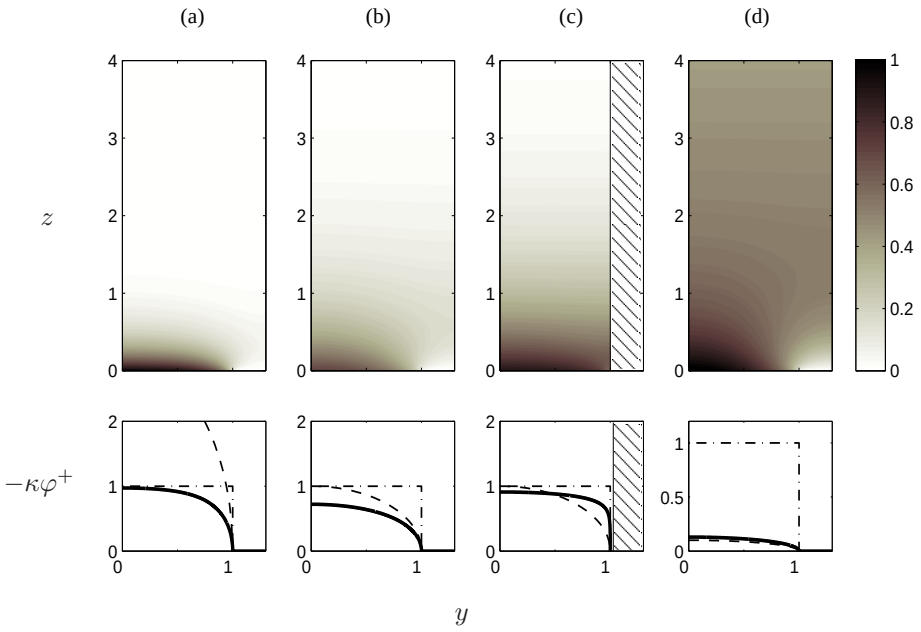

Figure 4: Filled contours representing levels of $-\kappa\varphi$ in the (y, z) space (above) and corresponding values at $z = 0^+$ plotted as function of y (below, bold lines), for four typical sets of parameters κ and d; (a), $\kappa = 5$ and $d = 0.3$; (b), $\kappa = 1$ and $d = 0.3$; (c), $\kappa = 1$ and $d = 10^{-4}$; (d), $\kappa = 0.1$ and $d = 0.3$. Dashed lines and dashed-dotted lines indicates value of $-\kappa\varphi^+$ predicted by the slender-body and two-dimensional theories respectively [see equations (23) and (24)]. The values have been multiplied by 8 in the color plot of case (d) in order to improve the visibility.

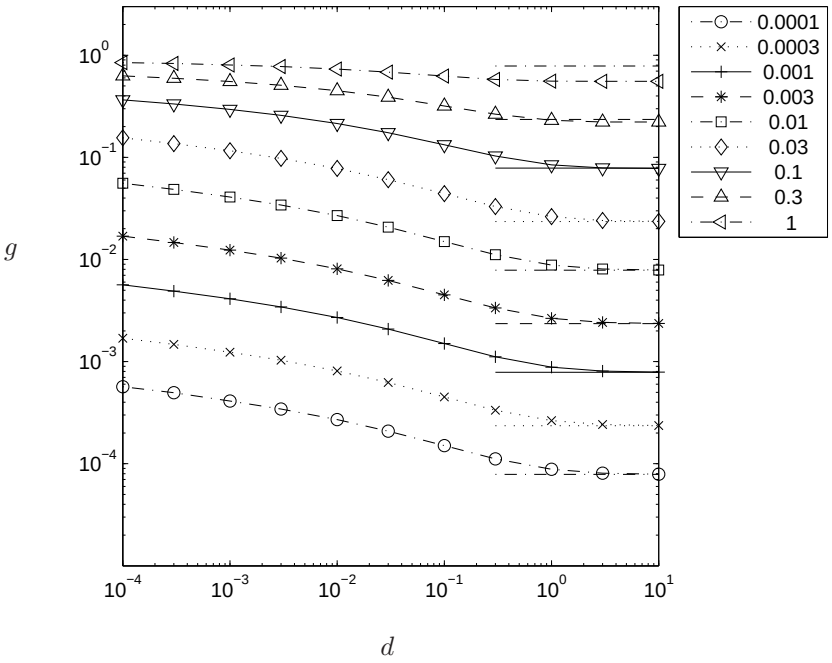

Figure 5: Value of $g = -\kappa\langle\varphi^+\rangle$ as function of d for different values of the non-dimensional wavenumber κ. The values that have been effectively computed are given by marks. Horizontal segments indicates the value of g in the slender body limit. This limit correctly approximates the behavior of g for small values of κ ($\lesssim 0.1$).

decreasing κ has for consequence to approach the slender-body limit. These observations will be addressed more quantitatively in the following.

The value of g resulting from systematic numerical computations is now plotted in Fig. 5 as a function of the gap d for different values of the wavenumber κ between 10^{-3} and 1. Although accessible, higher values of κ have not been explored numerically because it requires strong mesh refinements. This limit will be addressed in the next section with an analytical approach. The values predicted by the slender-body theory are also plotted in Fig. 5 for comparison. The asymptotic limit for large d is recovered by the slender-body theory when κ is small enough, say $\kappa < 0.3$.

We are now looking for an empirical model describing the value of g for small κ and any value of the clearance d. In Fig. 6, the value of $4g/\pi\kappa - 1$ is plotted against d and shows that all points gather on a single curve when κ is smaller than 0.1. This means that g is of the form

$$g_{SB}(\kappa, d) = \frac{\kappa\,\pi}{4 f_{SB}(d)}, \quad \text{for } \kappa \ll 1, \tag{25}$$

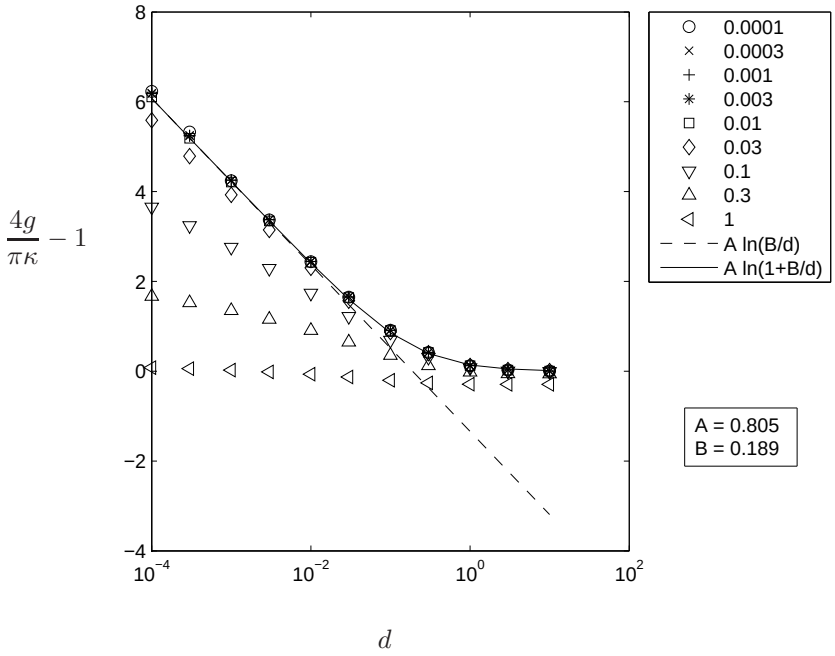

Figure 6: Value of $4g/\pi\kappa - 1$ as function of d with a log-linear scale, for different values of the non-dimensional wavenumber κ. Dashed line corresponds to the best linear fit of the dataset when $\kappa \leq 0.1$. Solid line is the approximation for g given by equation (25).

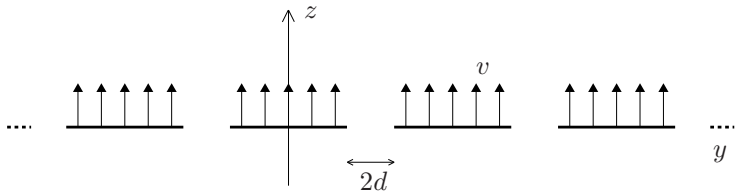

Figure 7: Schematic representation of the equivalent problem in the Fourier space using the mirror symmetry.

where f_{SB} can be determined by fitting the numerical results

$$f_{SB}(d) \approx \left[1 + 0.805 \ln\left(\frac{d + 0.189}{d}\right)\right]^{-1}. \tag{26}$$

Equation (25) describes the extension of the slender-body theory to account for the presence of the walls. It is valid for any value of the clearance d as long as κ is small enough ($\kappa < 0.1$), that is when the wavelength of the deflection is large compared to the plate span.

3.2. Theoretical calculation

As illustrated in Fig. 7, the Helmotlz problem of a plate moving at constant velocity between two boundaries given by equations (19-21) can be transformed by replacing the walls by mirror symmetry planes. The equivalent problem is thus an infinite number of similar plates separated by a distance $2d$ all moving at the same constant velocity v.

Using the Green's representation theorem, the perturbation potential satisfies

$$\varphi(y, z) = \int_{S_p} [\varphi](\eta) \left[\partial_\zeta H(y, z, \eta, \zeta)\right]_{\zeta=0} \mathrm{d}\eta, \tag{27}$$

where S_p is the plate surfaces, $[\varphi]$ is the potential jump across the plate (i.e. $[\varphi](y) = \varphi(y, 0^+) - \varphi(y, 0^-)$ and H is the Green function of the Helmoltz equation in two dimensions

$$H(y, z, \eta, \zeta) = \frac{1}{2\pi} K_0\left(\kappa\sqrt{(y - \eta)^2 + (z - \zeta)^2}\right), \tag{28}$$

with K_ν the modified Bessel function of the second kind.

Differentiating equation (27) with respect to z and taking the limit $z = 0$ yields

$$\left[\varphi_z\right]_{z=0} = \fint_{S_p} [\varphi](\eta) F(|y - \eta|) \mathrm{d}\eta = 1, \quad \text{for } |y| < 1, \tag{29}$$

where the cross on the integral sign stands for the integration in the finite part sense (Hadamard, 1932; Mangler, 1951) and the kernel is

$$F(y) = \frac{\kappa K_1(\kappa y)}{2\pi y}. \tag{30}$$

Here the integration is not defined in the usual sense because the kernel $F(y)$ behaves like $1/(2\pi y^2)$ in the limit of small y.

The inverse problem (29) can be solved numerically for a given value of the wavenumber κ. To do that, the potential jump $[\varphi]$ is expanded on even Chebyshev polynomials of the second kind such that

$$[\varphi](y) = \sqrt{1-y^2}\sum_{i=1}^{\infty} A_i U_{2i-2}(y), \tag{31}$$

where the prefactor $\sqrt{1-y^2}$ ensures the correct behavior as $|y| \to 1$. Inserting the expansion (31) into equation (29) and evaluating the discrete scalar product with the Chebyshev polynomials of the first kind $T_j(y)$ leads to a linear system for the vector (A_i) which can be solved numerically. The averaged potential jump along the plate span is then given by $\langle[\varphi]\rangle_y = -\pi A_1/2$ and therefore the function g is

$$g(\kappa, d) = \frac{\pi\kappa}{4} A_1(\kappa, d). \tag{32}$$

The theoretical method described here to calculate the averaged potential jump $\langle[\varphi]\rangle$ is complementary to the numerical method described above. It allows to carry out the calculation in the limit of large wavenumber κ and small gap d with the product κd asymptotically small. When κ is small however, the number of plate replicas needed to obtain an accurate calculation of the potential varies as $1/\kappa$. The present theoretical method is therefore not pertinent in this limit.

Examples of such calculations are given in Fig. 8 where the averaged potential jump is given as a function of the gap d for different wavenumbers κ. For large clearance d, the large span approximation obtained by Eloy et al. (2007) is recovered

$$g(\kappa, d) \simeq 1 - \frac{1}{2\kappa}, \quad \text{for } d \gg 1,\ \kappa \gg 1. \tag{33}$$

Let us now estimate the function of g in the limit large κ for any value of d. In Fig. 9, $(1 - g/2\kappa)$ is plotted as a function of κd with a logarithmic scale. All the points gather on a single curve showing that, in the large-span limit, g is of the form

$$g_{LS}(\kappa, d) \simeq 1 - \frac{f(\kappa d)}{2\kappa}, \quad \text{for } \kappa \gg 1. \tag{34}$$

where $f(\kappa d)$ behaves as a power law for small values of κd. An empirical evaluation of this function can be found by fitting the results and yields

$$f(x) \approx \left(1 + \frac{0.18}{x^2}\right)^{-0.075}. \tag{35}$$

The equation (34), where f is given by (35), will be referred to as the large span approximation for $g(\kappa, d)$, valid for any value of the clearance d and large value of the wavenumber κ, that is when the deflection wavelength is small compared to the plate span.

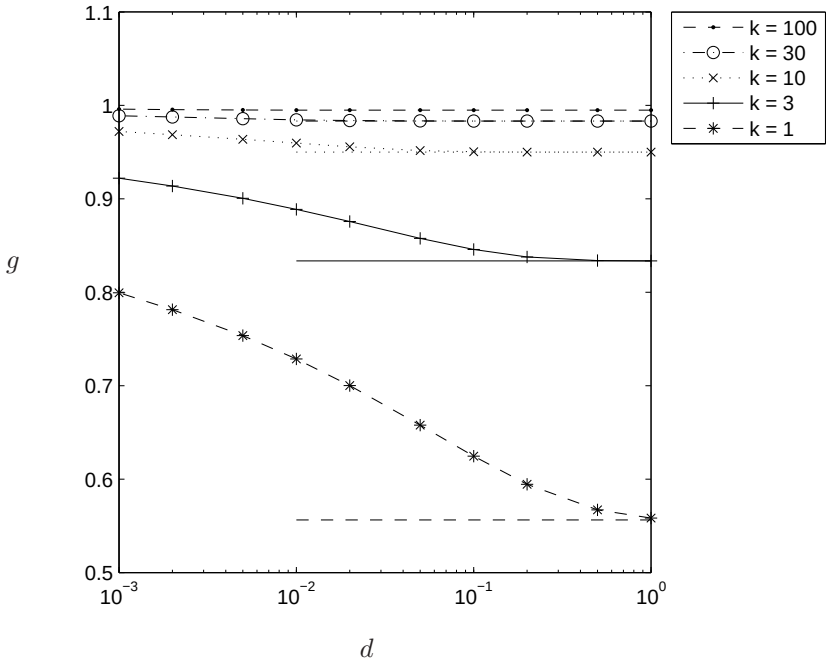

Figure 8: Function g as a function of the gap d for different values of the wavenumber κ. The horizontal lines correspond to the limit $d \gg 1$ and the segments between symbols are just guides for the eye.

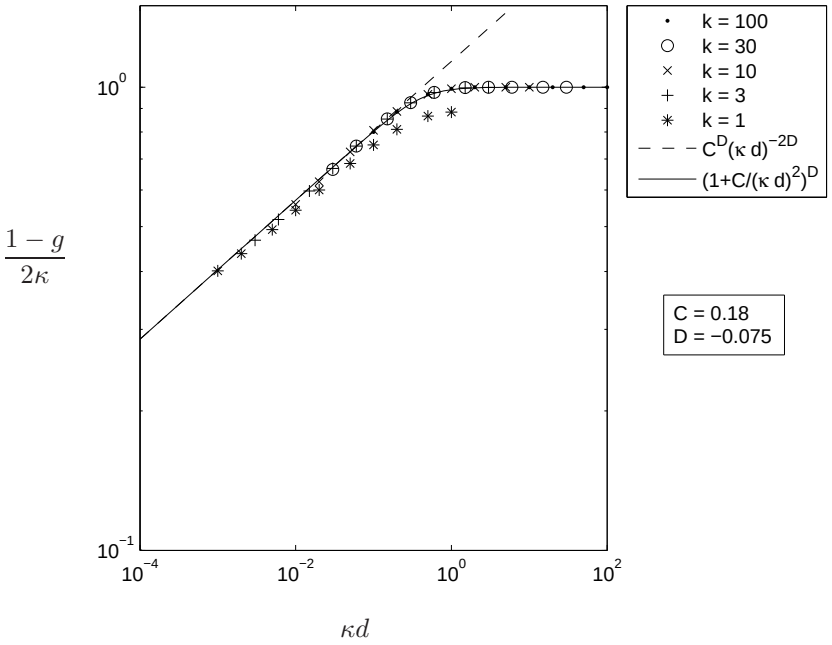

Figure 9: Function $1 - g/2\kappa$ as a function of κd for different values of the wavenumber κ. The dashed line shows the power law $1.14(\kappa d)^{0.15}$ and the solid line represents the approximation of g given by equation (34) where f is given by (35).

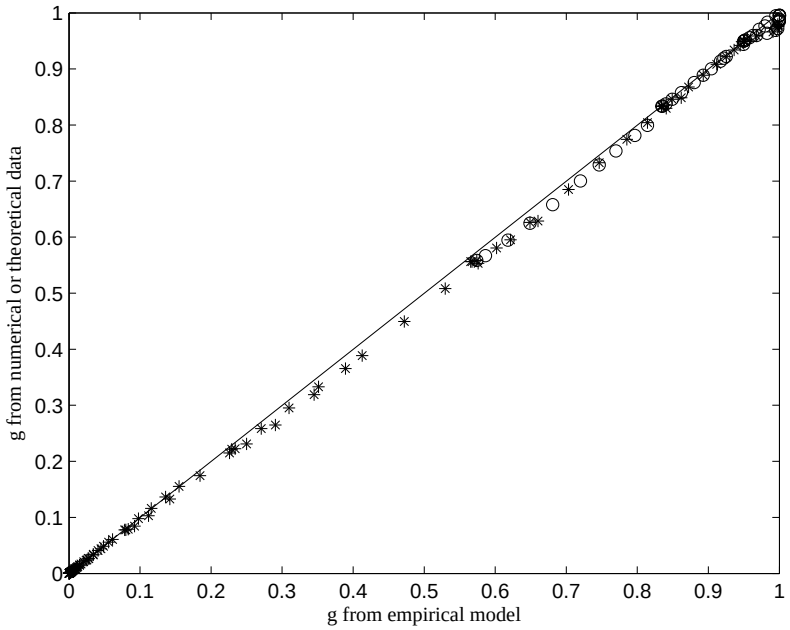

Figure 10: Complete dataset of the numerical and theoretical values of the averaged pressure jump g, plotted as function of the empirical model g_e given by equation (36); (*), numerical data; (o), theoretical data.

3.3. Empirical model for the pressure jump

In sections 3.1 and 3.2 we have derived empirical models for the function $g(\kappa, d)$, valid for small and large values of κ respectively. A good approximation for all values of κ can be obtained from a composite extension of these two empirical models,

$$g_e(\kappa, d) = 1 - \left[\frac{1}{1 - g_{LS}} + \exp\left(g_{SB} - \frac{1}{1 - g_{LS}} \right) \right]^{-1}, \tag{36}$$

where the functions g_{SB} and g_{LS} are given by the equations (25) and (34) respectively.

To assess the validity of the above approximation for g, the entire dataset of numerical and theoretical values of the pressure jump g is plotted as a function of g_e in Fig. 10. All symbols lie on the line $g = g_e$, indicating that the empirical model given by equation (36) correctly predicts the pressure jump with a maximum error of 8% at any value of κ and d.

To solve the problem in the real space, the Fourier transform of $1/g_e$ is now evaluated to obtain the kernel G given by equation (18). It yields

$$G(x, h, c) \approx \frac{1}{x} + \mathrm{sgn}(x) \left[\frac{\pi}{2} \frac{f_{LS}\left(|x|/c\right)}{h + 2|x|} + \left(\frac{4}{h} - \frac{4}{h + 2|x|} \right) f_{SB}(2c/h) \right], \tag{37}$$

where the function f_{SB} is given by equation (26) and

$$f_{LS}(x) \approx (1 + 0.5x)^{-0.16}. \tag{38}$$

The functions f_{SB} and f_{LS} describe in the slender-body and large-span limit the effect of channel confinement. For an asymptotically large channel (i.e. $c \gg 1$), these functions are equal to one and the kernel $G(x, h, c)$ found in Eloy et al. (2007, 2008) is recovered. On the other hand, when the clearance c goes to zero, these two functions decrease and therefore the kernel G tends to $1/x$ which is the two-dimensional limit.

4. Stability analysis

4.1. Galerkin decomposition

Similarly to what was done by Eloy et al. (2007, 2008), the stability analysis is performed by assuming a complex frequency ω, and decomposing the plate deformation on Galerkin modes

$$w(x, t) = \mathrm{e}^{\mathrm{i}\omega t} \sum_i a_i w_i(x), \tag{39}$$

where the spatial Galerkin modes $w_i(x)$ are the eigenmodes of a clamped-free beam in vacuo in order to satisfy the boundary conditions in $x = 0$ and $x = 1$.

Inserting the decomposition (39) into equation of motion (3) and executing scalar products with the modes $w_j(x)$ yields a linear problem for the unknown amplitude vector $\{a_i\}$. This eigenvalue problem admits a non trivial solution only if the determinant of the linear operator is zero which is achieved for discrete values of the complex frequency $\{\omega_i\}$. The real part of these frequency gives the angular frequency of the oscillations and its imaginary part gives the mode growth rate $\sigma = -\Im(\omega)$. For a given eigenmode, the growth rate is a function of the dimensionless parameters of the problem: the reduced velocity U^*, the mass ration M^*, the aspect ratio h and the dimensionless clearance c. The aim of the stability analysis is to find, for a given set of parameters (M^*, h, c), the critical value of the reduced velocity ${U^*}_c(M^*, h, c)$ above which at least one mode is unstable (i.e. has a positive growth rate σ).

4.2. Solution for the pressure

The solution for the inverse problem (17) is sought for a given Galerkin mode w_i

$$\frac{1}{2\pi} \fint_0^1 p_i'(\xi) G(x - \xi, h, c) \, \mathrm{d}\xi = (\mathrm{i}\omega + \mathrm{d}_x)^2 \, w_i, \tag{40}$$

where G is given by (37), by expanding p_i' on Chebyshev polynomials such that

$$p_i'(x) = \sum_{j=1}^{\infty} A_{ij} \frac{T_j(2x - 1)}{\sqrt{x(1 - x)}}, \tag{41}$$

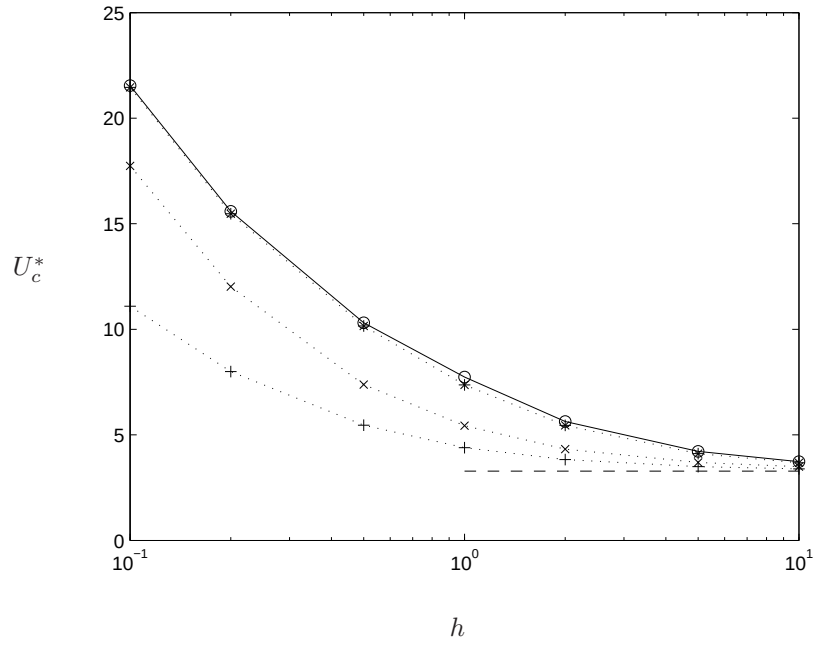

Figure 11: Critical velocity as a function of the aspect ratio h for a mass ratio $M^* = 0.5$. The different symbols correspond to different gaps: $c = \infty$ (circle), $c = 1$ (star), $c = 10^{-2}$ (crosse), $c = 10^{-4}$ (plus); and the dashed line corresponds to the two-dimensional limit $h = \infty$.

thus assuming an inverse square-root singularity at the leading and trailing edge for p_i'. In this expansion, T_j are the Chebyshev polynomials of the first kind.

Inserting (41) into equation (40) and applying a scalar product with the Chebyshev polynomials of the second kind $U_k(2x-1)$ leads to a linear problem for A_{ij} which is solved numerically for given values of the geometrical parameters h and c. The averaged pressure jump $\langle [p_i] \rangle$ is then found by integrating p_i' given by equation (41). This leads to no singularity on the leading and trailing edges (as the averaged pressure jump goes as $x^{1/2}$). As it has been discussed in Eloy et al. (2008), it is not physically correct as one expects the pressure jump to have an inverse square-root singularity at the leading edge. However, it has been shown in the same paper that taking into account this leaging-edge singularity do not modify greatly the stability characteristics as the leading edge is clamped and the pressure forces do not work at this position.

In practice, 15 Galerkin modes and 20 Chebyshev polynomials have been used in the following computations.

4.3. Results

Now that the average pressure jump $\langle [p_i] \rangle$ for a given Galerkin mode w_i can be found by inverting the problem (40), we are able to compute the eigenmodes

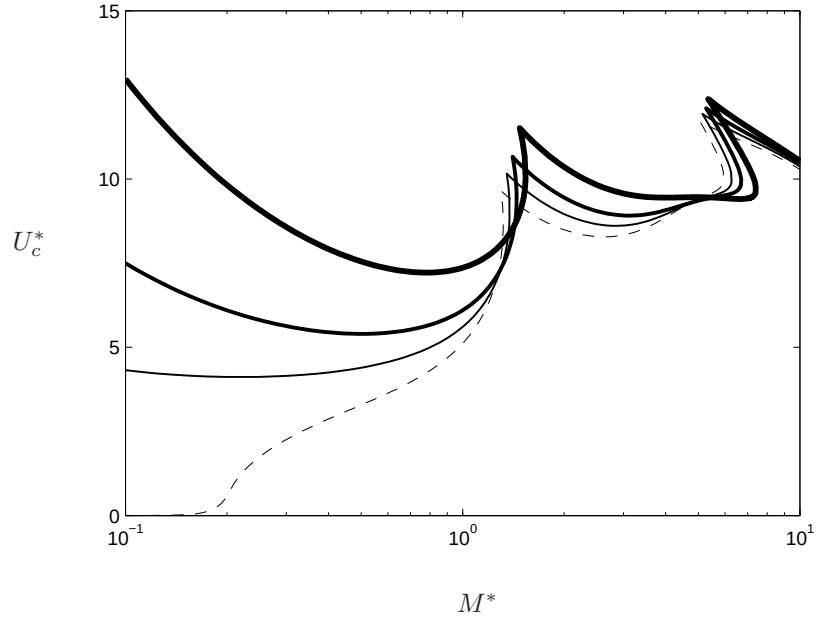

Figure 12: Critical velocity as a function of the mass ratio M^* for an aspect ratio $h = 1$. The different thicknesses correspond to different gaps: $c = \infty$ (thick), $c = 10^{-2}$ (medium), $c = 10^{-4}$ (thin); and the dashed line corresponds to the two-dimensional limit $h = \infty$.

of the equation of motion (3) and their complex eigenfrequecies ω. Looking at the imaginary part of the eigenfrequencies, the critical velocity ${U^*}_c$ can also be computed as a function of the dimensionless parameters M^*, h and c. Examples of such calculations are showed in Figs. 11 and 12 where the critical velocity is first plotted as a function of the aspect ratio for a fixed mass ratio, and then as a function of the mass ratio for a given aspect ratio. Each time, the critical velocity is computed for different values of the clearance c.

Figures 11 and 12 show the effect of confinement on the flutter instability. The first thing to notice is that the characteristics of the instability are not modified qualitatively by the presence of the walls. As expected, the threshold converges smoothly towards the two-dimensional limit as the clearance is reduced. It also appears that when the clearance c is larger than 1, the critical velocity is the same as in the case of an open flow ($c \gg 1$). When c is reduced, the critical velocity always lies between the open-flow and two-dimensional limits and converges very slowly towards the two-dimensional limit.

For a relatively small mass ratio ($M^* = 0.5$), Fig. 11 show the effect of the aspect ratio on the instability. As it has already been discussed in Eloy et al. (2008) for an open flow ($c \gg 1$), if all the other parameters are kept constant, the smaller the span is, the more stable is the system. This assertion holds

also when the plate is confined between two walls and the clearance c is kept constant.

For a square plate ($h = 1$), Fig. 12 show the influence of the mass ratio on the instability threshold. This stability diagram exhibits several lobes corresponding to different eigenmodes. For $M^* \lesssim 1.5$, the second mode is the most unstable (assuming that the modes are ordered with increasing frequency). Note that, classically, the first mode is always stable for these clamped-free boundary conditions (see Païdoussis, 2004, for instance). For $1.5 \lesssim M^* \lesssim 6$, the third eigenmode is the most unstable, and so on. The effect of confinement does not modify this picture significantly. Figure 12 also show that for large mass ratios, all the curves converge towards ${U^*}_c \approx 10$, for all values of the clearance. This is due to the fact that the number of mode wavelengths along the plate chord increases as M^* increases. The dimensionless wavenumber κ introduced in section 3 thus increases and the pressure jump converges towards its two-dimensional limit.

5. Discussion

In this article, the effect of channel clearance on the flow-induced instability of a cantilevered flat plate has been addressed. Numerical and theoretical calculations were performed to obtain the pressure distribution around the plate in the Fourier space as function of the various parameters. Using these numerical and theoretical data, an empirical model for the pressure jump has been derived. This model allowed to compute the eigenfrequencies of the coupled flow-structure problem. Critical velocities for the flutter instability as a function of the different parameters of the problem have then been computed. As expected, when the clearance is reduced to zero, the critical velocity was found to approach the limit predicted by a two-dimensional model. However, this limit was found to be reached only for very small values of the clearance. Indeed for a value as small as $c = 10^{-4}$, a large discrepancy between the two-dimensional model and our empirical model persists. The mass ratio effect has also been investigated, and it has been observed that the influence of the rigid walls is more pronounced for relatively heavy and rigid plates (i.e. $M^* < 1$).

These results raise the following question: for heavy and rigid plates, is the comparison between two-dimensional models and experiments relevant ? Indeed, the value of the clearance would have to be far smaller than 10^{-4}, which is unattainable experimentally. Among the works that investigated experimentally the flutter of plates in channel flow, the values of the clearance can be estimated to be $\mathcal{O}(1)$ (Yamaguchi et al., 2000) or $\mathcal{O}(10^{-2})$ (Huang, 1995). Our results indicate that the flow in these experimental studies cannot be considered two-dimensional to correctly predict critical velocities for such values of the clearance. In the work of Aurégan and Depollier (1995), the clearance has a value of approximately 10^{-2} (Aurégan, 2010), and the same recommendation should apply. But here, the channel confinement in the Y-direction is also important, which effect can be roughly estimated as an increase of the mass ratio M^*. The present article shows that this has for consequence to reduce the

influence of the channel clearance. A two-dimensional model has hence more chances to give satisfying results in this case. Regarding the experimental work of Watanabe et al. (2002b), our model is probably not applicable in this case because the authors observed three-dimensional deformations of the paper sheet when small clearance values of order 10^{-2} were attained. This is not compatible with our one-dimensional deformation hypothesis. In conclusion, the only cases where a two-dimensional approximation is pertinent are the very long and/or very flexible plates (i.e. $M^* \gg 1$) or the soap film experiments such as the experimental work of Zhang et al. (2000).

These observations indicates that an experimental work focusing on the effect of channel clearance would be necessary to complement the theoretical results of the present article. Also, extending our model to take into account the confinement in the transverse direction would bring some insight into the instability phenomenon, and would fill the gap between the flag-type problem and the snoring or leakage flow problems.

References

Alben, S., Shelley, M.J., 2008. Flapping states of a flag in an inviscid fluid: Bistability and the transition to chaos. Physical Review Letters 100, 074301.

Aurégan, Y., 2010. Private Communication.

Aurégan, Y., Depollier, C., 1995. Snoring: Linear stability and in-vitro experiments. Journal of Sound and Vibration 188, 39–53.

Balint, T.S., Lucey, A.D., 2005. Instability of a cantilevered flexible plate in viscous channel flow. Journal of Fluids and Structures 20, 893–912.

Datta, S., Gottenberg, W., 1975. Instability of an elastic strip hanging in an airstream. Journal of Applied Mechanics 42, 195–198.

Eloy, C., Lagrange, R., Souilliez, C., Schouveiler, L., 2008. Aeroelastic instability of cantilevered flexible plates in uniform flow. Journal of Fluid Mechanics 611, 97–106.

Eloy, C., Souilliez, C., Schouveiler, L., 2007. Flutter of a rectangular plate. Journal of Fluids and Structures 23, 904–919.

Guo, C.Q., Paidoussis, M.P., 2000. Stability of Rectangular Plates With Free Side-Edges in Two-Dimensional Inviscid Channel Flow. Journal of Applied Mechanics 67, 171–176.

Hadamard, J., 1932. Lectures on Cauchy's problem in linear differential equation. Dover, New York.

Howell, R.M., Lucey, A.D., Carpenter, P.W., Pitman, M.W., 2009. Interaction between a cantilevered-free flexible plate and ideal flow. Journal of Fluids and Structures 25, 544–566.

Huang, L., 1995. Flutter of cantilevered plates in axial flow. Journal of Fluids and Structures 9, 127–147.

Kornecki, A., Dowell, E.H., O'Brien, J., 1976. On the aeroelastic instability of two-dimensional panels in uniform incompressible flow. Journal of Sound and Vibration 47, 163–178.

Lemaitre, C., Hémon, P., de Langre, E., 2005. Instability of a long ribbon hanging in axial air flow. Journal of Fluids and Structures 20, 913–925.

Lighthill, M., 1960. Note on the swimming of slender fish. Journal of FLuid Mechanics 9, 305–317.

Mangler, K.W., 1951. Improper integrals in theoretical aerodynamics. Tech. Rep. Aero 2424. British Aeronautical Research Council.

Michelin, S., Llewellyn Smith, S.G., 2009. Linear stability analysis of coupled parallel flexible plates in an axial flow. Journal of Fluids and Structures 25, 1136–1157.

Michelin, S., Llewellyn Smith, S.G., Glover, B.J., 2008. Vortex shedding model of a flapping flag. Journal of Fluid Mechanics 607, 109–118.

Païdoussis, M.P., 2004. Fluid-structure Interactions. Slender Structures and Axial Flow. volume 2. Academic Press.

Rayleigh, L., 1879. On the instability of jets. Proc. London Mat. Soc. X, 4–13.

Taneda, S., 1968. Waving motions of flags. Journal of the Physical Society of Japan 24, 392–401.

Tang, L., Païdoussis, M.P., 2007. On the instability and the post-critical behaviour of two-dimensional cantilevered flexible plates in axial flow. Journal of Sound and Vibration 305, 97–115.

Theodorsen, T., 1935. General theory of aerodynamic instability and the mechanism of flutter. NACA Report 496.

Watanabe, Y., Isogai, K., Suzuki, S., Sugihara, M., 2002a. A theoretical study of paper flutter. Journal of Fluids and Structures 16, 543–560.

Watanabe, Y., Suzuki, S., Sugihara, M., Sueoka, Y., 2002b. An experimental study of paper flutter. Journal of Fluids and Structures 16, 529–542.

Wu, X., Kaneko, S., 2005. Linear and nonlinear analyses of sheet flutter induced by leakage flow. Journal of Fluids and Structures 20, 927–948.

Yamaguchi, N., Sekiguchi, T., Yokota, K., Tsujimoto, Y., 2000. Flutter Limits and Behavior of a Flexible Thin Sheet in High-Speed Flow– II: Experimental Results and Predicted Behaviors for Low Mass Ratios. Journal of Fluids Engineering 122, 74–83.

Zhang, J., Childress, S., Libchaber, A., Shelley, M., 2000. Flexible filaments in a flowing soap film as a model for one-dimensional flags in a two-dimensional wind. Nature 408, 835–839.